On the compressibility and poroelasticity of human and murine skin

Journal Article

Author(s):
Wahlsten, Adam (iD); Pensalfini, Marco (iD); Stracuzzi, Alberto (iD); Restivo, Gaetana; Hopf, Raoul; Mazza, Edoardo

On the Compressibility and Poroelasticity of Human and Murine Skin

Adam Wahlsten[★] · **Marco Pensalfini**[★] · **Alberto Stracuzzi** ·
Gaetana Restivo · **Raoul Hopf** · **Edoardo Mazza**

Abstract A total of 37 human and 33 murine skin samples
were subjected to uniaxial monotonic, cyclic, and relaxation
experiments. Detailed analysis of the three-dimensional kine-
matic response showed that skin volume is significantly re-
duced as a consequence of a tensile elongation. This behavior
is most pronounced in monotonic but persists in cyclic tests.
The dehydration associated with volume loss depends on
the osmolarity of the environment, so that tension relaxation
changes as a consequence of modifying the ionic strength
of the environmental bath. Similar to *ex vivo* observations,
complementary *in vivo* stretching experiments on human
volar forearms showed strong in-plane lateral contraction.
A biphasic homogenized model is proposed which allows
representing all relevant features of the observed mechanical
response.

AW and MP share first authorship of this article

A. Wahlsten (✉) · M. Pensalfini · A. Stracuzzi
Institute for Mechanical Systems, Department of Mechanical and Process
Engineering, ETH Zurich,
8092 Zurich, Switzerland
E-mail: wahlsten@imes.mavt.ethz.ch

G. Restivo
Department of Dermatology, University Hospital Zurich,
8091 Zurich, Switzerland

R. Hopf · E. Mazza (✉)
Institute for Mechanical Systems, Department of Mechanical and Process
Engineering, ETH Zurich,
8092 Zurich,
Switzerland
Empa, Swiss Federal Laboratories for Materials Science and Technology,
8600 Dübendorf, Switzerland
E-mail: mazza@imes.mavt.ethz.ch

1 Introduction

The skin is the outermost organ of the human body, contribut-
ing essential homeostatic and protective functions (Limbert,
2017). The interaction of multiple biochemical factors (en-
zymes, growth factors, hormones, proteins) and the complex
network of regulatory signals (Kitano, 2002; Page-McCaw
et al., 2007) determine the tissue characteristics and their
evolution in processes such as growth and remodeling (Eskan-
dari and Kuhl, 2015; Page-McCaw et al., 2007), aging (Imai,
2009), reaction to mechanical stimuli (Wang et al., 2015), or
the actuation of a defense in response to insults (Buganza
Tepole, 2017; Wang et al., 2015).

While the traditional view of soft biological tissue func-
tion is centered around cell activities, increasing evidence
speaks to a comparable role of the extracellular matrix (ECM)
in mediating and delivering bio-chemo-mechanical cues
(Humphrey et al., 2014; Mouw et al., 2014). These con-
tribute to or even direct cell behavior (Achterberg et al., 2014;
Guilak et al., 2009; Lukashev and Werb, 1998; Rosso et al.,
2004; Tracy et al., 2016). Soft tissues are in fact multiphasic
materials, where cells are hosted within a hydrated matrix
comprised of matricellular proteins which interact in cell-
matrix signaling (Tracy et al., 2016). In particular, elastin and
collagen provide the ECM with a reticular structure, while
proteoglycans and glycosaminoglycans (GAGs) contribute by
creating a charged, dynamic, osmotically driven interstitial
space (Tracy et al., 2016), containing both fixed and mobile
ions (Lai et al., 1991; Lanir, 2017). Collagen, constituting up
to 77 % of the fat-free dry weight of human skin (Tracy et al.,
2016), dominates the ECM composition and is traditionally
associated with the mechanical behavior of skin. However,
recent investigations on human amnion, bovine Glisson's
capsule, and porcine pericardium (Ehret et al., 2017) sug-
gested an equally important contribution of interstitial fluid
(IF) mobility to the biophysical characteristics of the ECM.

This relation between macroscopic tissue deformation and IF flow remains largely under-investigated in skin, where additional complexity arises from the presence of multiple layers, *i.e.* stratum corneum, viable epidermis, and papillary and reticular dermis (Kolarsick et al., 2011).

As the skin is primarily subjected to tensile stresses in the membrane plane, several studies have investigated the mechanical behavior of excised tissue under uniaxial (Bancelin et al., 2015; Ehret et al., 2011; Har-Shai et al., 1996; Muñoz et al., 2008; Ní Annaidh et al., 2012b; Wong et al., 2016) or biaxial (Groves et al., 2013; Hollenstein et al., 2011; Lanir and Fung, 1974; Tonge et al., 2013a) tension. Early work have shown that the characteristic J-shaped stress-stretch response of skin is due to progressive reorientation of collagen fibers toward the direction of loading (Brown, 1973; Gibson et al., 1965). This microstructural mechanism has been observed to cause a large lateral contraction perpendicular to the loading direction for soft collagenous membranes (Bircher et al., 2016; Buerzle and Mazza, 2013) as well as for the skin (Gibson et al., 1965; Jayyosi et al., 2017; Stark and Al-Haboubi, 1980). In fact, for materials consisting of a 3D fiber network microstructure, uniaxial tension can result in large reductions of specimen cross-sectional area and volume, as experimentally shown for articular cartilage (Woo et al., 1979), collagen gels (Lake and Barocas, 2011), fibrin gels (Brown et al., 2009), and recently for amnion, Glisson's capsule, and pericardium (Bircher et al., 2016; Ehret et al., 2017; Mauri et al., 2015b). This behavior has been rationalized by numerical models involving discrete fiber networks (Ehret et al., 2017; Picu et al., 2018). Similar experimental investigations have been conducted on the skin (Gibson et al., 1965; Stark and Al-Haboubi, 1980; Veronda and Westmann, 1970), suggesting that, as the tissue starts to carry larger tensile loads, volume is reduced due to expulsion of IF. However, the majority of recent efforts to establish corresponding biomechanical models has been based on the assumption of incompressibility (*e.g.,* Buganza Tepole et al., 2014; Ehret et al., 2011; Hendriks et al., 2006; Limbert, 2011; Ní Annaidh et al., 2012a; Tonge et al., 2013b; Rubin and Bodner, 2002; Weickenmeier et al., 2015), as thoroughly reviewed by Benítez and Montáns (2017) and Limbert (2017). For highly hydrated materials, this appears only justified if the IF is bound to the solid matrix, at least during the considered loading history (Lanir, 2017), or if the specimen is fully confined by impermeable surfaces (North and Gibson, 1978). Conversely, load support by the interstitial fluid pressure (IFP) and time-dependent poroelastic effects have been recognized as important mechanisms in skin under compressive loading (Daly, 1982; Bader and Bowker, 1983; Oomens et al., 1987), followed by the development of biphasic models to rationalize compression and indentation experiments (Mak et al., 1994; Oftadeh et al., 2018; Oomens et al., 1987).

In light of this evidence on the composition, function, and mechanical behavior of soft collagenous tissues, we present a critical analysis of the contribution of the IF to the macroscopic deformability of human and murine skin under uniaxial tensile loading, corroborated by the use of a biphasic constitutive model of soft tissue behavior. Our results show that: (i) skin is compressible, losing volume upon increased tension; (ii) this phenomenon is reversible over multiple loading-unloading cycles; (iii) the in-plane lateral contraction upon tissue extension is also evident *in vivo*; (iv) the tension arising from tissue extension can be controlled by altering the osmolarity of the fluid environment—and conversely, change in volume due to applied tension alters the ionic environment inside the skin. These findings add to the current understanding of the complex environment hosting skin cells by suggesting a direct link between tissue stretching, local volume changes, and perturbation of the homeostatic state via alterations of the chemo-physical characteristics of the ECM.

2 Materials and Methods

2.1 Sample preparation

Human abdominal- and breast-skin biopsies were provided from the University Hospital Zurich with assistance of the Skintegrity biobank. All material were surplus biopsies from four female donors between 32 and 50 years of age who underwent surgery and provided signed informed consent that was approved by the local institutional review board (EK 647 and EK 800). The use of surplus skin for biomechanical experiments had been approved by the Ethical Committee of Canton Zurich (BASEC ID: 2017-00684). The tissue was kept in phosphate-buffered saline solution on ice until used for mechanical testing, performed within 24 hours of biopsy collection.

7-8 weeks old C57BL/6 wild-type male mice, housed in accordance with Swiss animal protection guidelines, were sacrificed by CO_2 inhalation. Their backs were shaved using clippers and marked with water-resistant ink to identify the cranio-caudal direction; the entire back skin was then carefully excised and excess fat was removed, as previously described (Pensalfini et al., 2018). Excised murine skin was kept in Dulbecco's Modified Eagle's Medium on ice until testing, performed during the same day as sacrifice.

Both human skin biopsies and murine back skins were placed on a graduated mat, and specimens with dimensions of 40×5 mm^2 (gauge dimensions: 20×5 mm^2) for uniaxial tension tests were prepared using a razor blade. An ink pattern was applied to the surface of human skin specimens using a waterproof pen (GeoCollege Pigment Liner 0.1) to facilitate identification of fiducial points for reconstruction of the local strain field (Sec. 2.2.1).

2.2 Mechanical characterization

Displacement-controlled uniaxial tension tests were performed using a custom-built setup (MTS Systems, Eden Prairie, MN, USA), consisting of horizontal hydraulic actuators equipped with force sensors with a capacity of 50 N and calibrated for a range of 20 N (Fig. 1a). Top-view images of the deforming specimen were captured at 2 Hz by a CCD-camera (Pike F-100B, Allied Vision Technologies GmbH, Stadtroda, Germany), equipped with a 0.25× telecentric lens (NT55-349, Edmund Optics Ltd., York, United Kingdom). All tests were performed at room temperature with specimens fully immersed in a physiological saline solution (0.15 M NaCl) during testing, unless otherwise specified. Three types of protocols—monotonic, cyclic, and relaxation—were employed for both human and murine specimens; Table 1 provides a summary of the *ex vivo* experimental campaign. Monotonic as well as cyclic tests were performed by imposing a nominal strain rate of $0.001\,\mathrm{s}^{-1}$. A series of ten loading-unloading cycles was prescribed for the cyclic tests; the start of each cycle was defined by a force threshold of 0.05 N from which specimens were extended to reach 20 % nominal strain as measured by clamp-to-clamp distance. In relaxation experiments, specimens were elongated at an imposed nominal strain rate of $0.05\,\mathrm{s}^{-1}$ until a pre-defined peak force (human: 1.0 N; murine: 0.5 N) was detected by the force sensors. Thereafter, the clamps were held in position for 30 minutes (human) or 5 minutes (murine) while force values were recorded. Additional relaxation experiments, incorporating a change in the salt concentration of the liquid environment (*cf.* Ehret et al., 2017), were included to analyze the influence of the osmolarity of the external bath[1] on the mechanical response. Imposing the same mechanical loading protocol as just described, the environmental bath container, initially containing 0.15 M NaCl, was rapidly emptied approximately 2 minutes after reaching the peak force and subsequently filled with either a hypertonic (0.60 M NaCl) or a hypotonic (distilled water, 0 M NaCl) solution.

Skin thickness contraction corresponding to specimen elongation was analyzed in additional monotonic uniaxial tensile tests using a custom-built stretching device (Mauri et al., 2015b), comprised of two stepper-motor-driven screws and a 7.5 N force sensor (DMS 7010, MTS Messtechnik Schaffhausen GmbH, Stein am Rhein, Switzerland) calibrated for a range of 5 N. Side-view images of the lateral surface of the specimen were taken by a CMOS-camera (EO-2323 Monochrome, Edmund Optics Ltd., York, United Kingdom) equipped with a 0.25× telecentric lens (NT55-349, Edmund Optics Ltd., York, United Kingdom), and synchronized acquisition of force, displacement, and images was accomplished through custom-written Matlab software (Matlab 2017a, The MathWorks, Inc., Natick, MA, USA). For optimal visual-

ization of the specimen thickness, these experiments were performed on specimens in air, kept moist with physiological saline solution during testing. Analysis of preliminary tests comparing the nominal tension and in-plane kinematics for moist and submerged murine skin specimens showed negligible influence of the different testing conditions, justifying the protocol adopted for the analysis of the out-of-plane kinematics. Murine skin specimens showed significant out-of-plane deflection of the free lateral edges due to a bending curvature in the plane perpendicular to the axis of elongation. This made an analysis of change in thickness difficult. To overcome this issue, the epidermal surface was treated with hair removal cream (Veet, Reckitt Benckiser Group plc, Slough, United Kingdom) and the specimen was placed on a soft, 0.5 mm thick, adhesive elastomer (VHB™4905, 3M™, Saint Paul, MN, USA), epidermis facing the synthetic material. This ensured that the lateral surface of murine specimens could be visualized clearly throughout the experiment, albeit to some extent constraining the in-plane contraction.
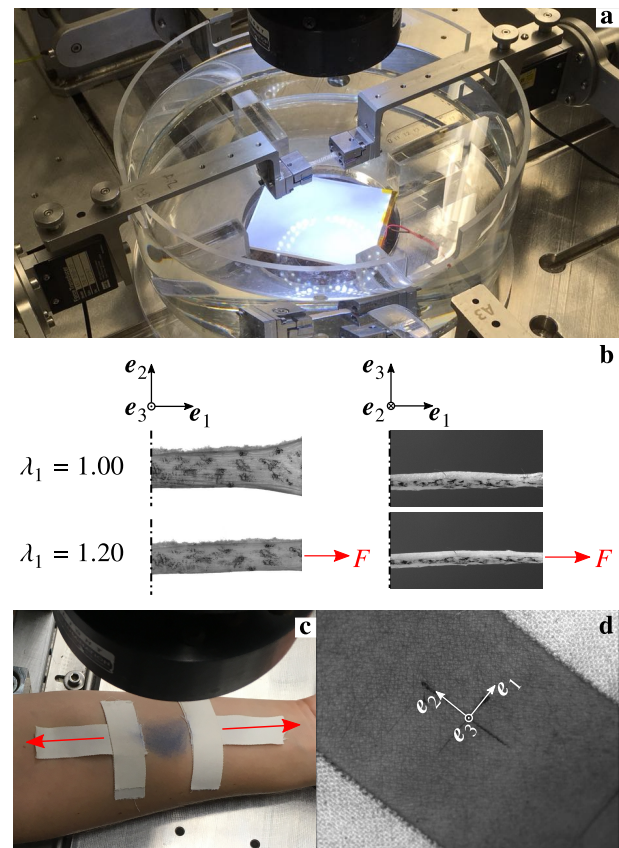
Fig. 1 Illustration of methods for *ex vivo* and *in vivo* mechanical characterization of human skin: (**a**) setup for uniaxial tensile testing with in-plane deformation analysis; (**b**) representative images from human skin experiments at reference ($\lambda_1 = 1.00$) and deformed ($\lambda_1 = 1.20$) length; (**c-d**) tape arrangement and applied ink pattern for *in vivo* stretching experiments

---

[1] A NaCl solution of salt concentration c_{ext} has the osmolarity $2c_{\mathrm{ext}}$.

Table 1 Summary of the number of specimens tested in the *ex vivo* experimental campaign

	Monotonic		Cyclic	Relaxation		
	In-plane	Out-of-plane		Control	0.6 M NaCl	Distilled Water
Human	9	7	5	6	5	5
Murine	7	4	6	6	5	5

2.2.1 Experimental data analysis

Due to the initial slack state of the specimens after clamping, the reference configuration for data post-processing was based on a force-threshold criterion. For the cyclic tests this coincided with the value defined in Sec. 2.2 (0.05 N), while values of 0.05 N (human) and 0.02 N (murine) were used for monotonic and relaxation tests. These values were selected as low as possible to ensure a taut but unstrained sample at the force threshold, as visible from the side-view images. The nominal tension, T, was computed by dividing the measured force values, F, by specimen gauge width, W: $T = F/W$. The local principal stretches (λ_i, $i = 1, 2, 3$) in the central region of the specimen were extracted from the acquired image sequences after reconstructing the displacements of fiducial points using a custom-written optical flow tracking algorithm (Hopf et al., 2016). Identification of reliable fiducial points was based on the ink pattern applied to the specimen surface (*cf.* Sec. 2.1) and inherent surface features.

Combining the mean in-plane, λ_2, and out-of-plane, λ_3, lateral contractions obtained from the monotonic experiments allowed computing the volume ratio, $J = \lambda_1\lambda_2\lambda_3$, as a function of specimen elongation λ_1. The local principal stretches were also used to evaluate the tangent Poisson's ratios ν_{1j} (Smith et al., 1999):

$$\nu_{1j} = -\frac{\partial \ln \lambda_j}{\partial \ln \lambda_1}, \quad j = 2, 3. \tag{1}$$

Elastic tensile moduli in the small deformation regime ($\lambda_1 \leq 1.02$) were estimated as $E = \frac{1}{H}\frac{\partial T}{\partial \lambda_1}$, H being the reference thickness; representative values for H were determined from the side-view images (human: 2 mm; murine: 0.5 mm). All numerical derivatives were computed by weighted least-squares fitting of a polynomial to the corresponding curve and extracting the analytical derivative of the polynomial. Experimental data are presented in terms of sample means with error bars corresponding to the square root of the estimated population variance.

2.3 *In vivo* planar kinematics of human skin

To assess the relevance of the *ex vivo* results for physiological tissue conditions, a protocol to evaluate the in-plane kinematics of human skin *in vivo* was further established. Two participants (a 29-year-old woman and a 27-year-old man) were recruited and provided signed informed consent; the procedure was approved by the ETH Zurich Ethics Commission (EK 2018-N-45). Following skin disinfection, strips of Leukotape® (BSN Medical GmbH, Hamburg, Germany) were placed on the subjects' volar forearms; this offered a simple system to apply modest deformation to the skin surface by pulling on the elements marked with red arrows in Fig. 1c. The tape bands were located roughly 30 mm apart, and an ink pattern (Pelikan Group GmbH, Berlin, Germany) was applied on the skin surface between them using a sponge in order to facilitate the reconstruction of the principal stretches based on the same algorithm mentioned in Sec. 2.2.1. Image sequences of the deforming skin surface were acquired at a frequency of 10 Hz, using the CCD-camera and telecentric lens described in Sec. 2.2. Note that, in the interest of safety, the deformation was applied by a human operator and its rate was thus not controlled; however, quantifications based on the recorded images showed typical values in the order of $1.5 \, \text{mm s}^{-1}$.

2.4 Constitutive model of skin biomechanics

A biphasic material model for skin was developed by extending previous work on the compressible and time-dependent response of soft collagenous biological membranes (Mauri et al., 2016; Ehret et al., 2017). The current work expands upon these models by including both elastic and dissipative contributions of the representative fibers, and by accounting for an initial swelling of the solid required to balance a non-zero osmotic pressure difference in a physiological environment.

2.4.1 Modeling framework

Based on the Theory of Porous Media (TPM), the skin was modeled as a homogenized saturated biphasic mixture, consisting of intrinsically incompressible solid and fluid constituents with current volume fractions φ_S and $\varphi_F = 1 - \varphi_S$, respectively (see, *e.g.*, Ehlers, 2002; Ehlers et al., 2009; Stracuzzi et al., 2018; Tomic et al., 2014). Osmotic effects, physically related to concentration differences due to the presence of fixed charges within the tissue (Huyghe and Janssen, 1997; Lai et al., 1991), were incorporated under the assumption of immediate equilibrium of ions compared to the time scales of the solid constituents and IF flow (Lanir, 1987;

Ehlers et al., 2009; Wilson et al., 2005a). Under quasi-static conditions and in the absence of body forces, the governing equations for the biphasic mixture read (Ehlers et al., 2009)

$$\operatorname{div}\left(\boldsymbol{v}_{\mathrm{S}} + \boldsymbol{q}\right) = 0, \tag{2a}$$

$$\operatorname{div}\boldsymbol{\sigma} = \boldsymbol{0}, \tag{2b}$$

where $\boldsymbol{v}_{\mathrm{S}}$ denotes the spatial velocity field of the solid particles, $\boldsymbol{q}$ the IF flux, and $\boldsymbol{\sigma}$ the Cauchy stress of the mixture. The IF flux, also labeled filter velocity, is defined as $\boldsymbol{q} = \varphi_{\mathrm{F}}(\boldsymbol{v}_{\mathrm{F}} - \boldsymbol{v}_{\mathrm{S}})$, $\boldsymbol{v}_{\mathrm{F}}$ being the spatial velocity field of the fluid particles (Ehlers et al., 2009). Although both phases are assumed intrinsically incompressible, the mixture may experience large volumetric deformations due to in- or efflux of fluid, as governed by volume balance of the mixture, see Eq. (2a).

When the tissue is in equilibrium with a physiological fluid environment (0.15 M NaCl), the osmotic pressure is generally non-zero and the corresponding fluid hydrostatic pressure is balanced by tension in the solid network (Ateshian et al., 2009; Azeloglu et al., 2008; Lai et al., 1991; Lanir, 2017; Maroudas, 1976; Wilson et al., 2005b). Thus, the *ex vivo* reference configuration—free of external forces and in equilibrium with a physiological saline solution—is not a zero-energy state. Assuming osmotic pressure is predominantly due to charge effects, the zero-energy configuration can be achieved by bringing an unloaded specimen in equilibrium with a solution of infinite salt concentration (Ateshian et al., 2009; Azeloglu et al., 2008; Lai et al., 1991). To distinguish between the zero-energy configuration and the *ex vivo* reference configuration, the approach by Hong et al. (2009), developed for isotropic, swelling gels, was adapted. The deformation gradient of the solid motion relative to the zero-energy configuration, $\mathbf{F}'$, was written as $\mathbf{F}' = \mathbf{FF}_0$. Here, $\mathbf{F}_0$ maps material line elements from the zero-energy configuration to the *ex vivo* reference through *free swelling*, whereas $\mathbf{F}$ is associated with subsequent deformations corresponding to those applied experimentally (Fig. 2). The decomposition facilitates a change of reference configuration, such that physical material parameters can be specified in the *ex vivo* reference configuration rather than in the experimentally unknown zero-energy configuration. The specific form of $\mathbf{F}_0$ depends on the material properties, and can, for homogeneous materials, be pre-computed from free-swelling equilibrium conditions (Hong et al., 2009; Lucantonio et al., 2013), hereby allowing simulations to be performed directly from the *ex vivo* reference configuration.

2.4.2 Constitutive equations

Following Ehlers et al. (2009), the Helmholtz free-energy density of the solid phase (per reference volume of the mixture in the zero-energy configuration) was additively split into mechanical and osmotic parts, $\Psi'(\mathbf{F}') = \Psi'_{\mathrm{S}}(\mathbf{F}') + \Psi'_{\mathrm{osm}}(\mathbf{F}')$,

whereas the fluid phase was considered inviscid. With respect to the volume of the mixture in the *ex vivo* reference, the free-energy density can be written as (Hong et al., 2009)

$$\Psi(\mathbf{F}) = \Psi_{\mathrm{S}}(\mathbf{F}) + \Psi_{\mathrm{osm}}(\mathbf{F}) = J_0^{-1}\Psi'(\mathbf{FF}_0), \quad J_0 = \det \mathbf{F}_0. \tag{3}$$

For this type of biphasic mixture, the Cauchy stress reads (Ehlers et al., 2009; Lanir, 1987; Wilson et al., 2005a)

$$\boldsymbol{\sigma} = \boldsymbol{\sigma}_{\mathrm{S}} - \left(\Delta\pi + \mu_{\mathrm{F}}\right)\mathbf{I}, \tag{4}$$

where $\boldsymbol{\sigma}_{\mathrm{S}}$ results from stored strain-energy Ψ'_{S}, $\mathbf{I}$ is the identity tensor, $\Delta\pi$ the osmotic pressure, and μ_{F} the fluid chemical potential; the resulting fluid hydrostatic pressure is thus $p = \mu_{\mathrm{F}} + \Delta\pi$ (Lanir, 1987).

The solid phase was modeled as a matrix-fiber composite with N representative fibers, spaced in an equiangular manner within the membrane plane to provide a quasi-isotropic response therein (Buerzle and Mazza, 2013), and possessing a small out-of-plane inclination angle ϑ, measured in the *ex vivo* reference configuration (Fig. 2). For all calculations, $N = 32$ fibers were used[2]. With respect to an orthonormal basis $\{\boldsymbol{e}_i\}_{i=1,2,3}$, the unit vectors describing fiber orientation in the *ex vivo* reference are given by

$$\boldsymbol{M}^i = \sin\theta\cos\phi^i\boldsymbol{e}_1 + \sin\theta\sin\phi^i\boldsymbol{e}_2 + \cos\theta\boldsymbol{e}_3, \tag{5}$$

with $\theta = \frac{\pi}{2} - \vartheta$ and $\phi^i = \frac{2\pi}{N}\left(i - \frac{1}{2}\right)$, $i = 1, 2, \ldots, N$. Energy stored in the solid phase by external mechanical work was defined by a Rubin-Bodner-type strain-energy function (Rubin and Bodner, 2002),

$$\Psi_{\mathrm{S}} = \varphi_{\mathrm{S}}^{\mathrm{ref}}\frac{\mu_0}{2q}\left(e^{qg} - 1\right), \quad g = g_{\mathrm{m}} + g_{\mathrm{fe}} + g_{\mathrm{fd}}, \tag{6}$$

where $\varphi_{\mathrm{S}}^{\mathrm{ref}}$ is the solid volume fraction in the *ex vivo* reference configuration and μ_0 and q are material parameters. The terms g_{m}, g_{fe}, and g_{fd} represent the contributions from a compressible neo-Hookean matrix and elastic (g_{fe}) and dissipative (g_{fd}) contributions of the fibers, respectively. These read

$$g_{\mathrm{m}} = m_1\left(\operatorname{tr}(\mathbf{Fb}_0\mathbf{F}^{\mathrm{T}}) - 3\right) + \frac{m_1}{m_2}\left((JJ_0)^{-2m_2} - 1\right), \tag{7a}$$

$$g_{\mathrm{fe}} = \frac{m_{\mathrm{fe}}}{m_4}\frac{1}{N}\sum_{i=1}^{N}\left\langle\lambda_{\mathrm{fe}}^i - 1\right\rangle^{2m_4}, \tag{7b}$$

$$g_{\mathrm{fd}} = \frac{m_{\mathrm{fd}}}{m_4}\frac{1}{N}\sum_{i=1}^{N}\left\langle\lambda_{\mathrm{fd}}^i - 1\right\rangle^{2m_4}, \tag{7c}$$

where $m_1, m_2, m_{\mathrm{fe}}, m_{\mathrm{fd}}$, and $m_4 \geq 1$ are material parameters, $\mathbf{b}_0 = \mathbf{F}_0\mathbf{F}_0^{\mathrm{T}}$, $J = \det \mathbf{F}$, and $\langle\cdot\rangle$ denotes Macauley brackets. The Cauchy stress $\boldsymbol{\sigma}_{\mathrm{S}}$ immediately follows as (*cf.* Mauri et al., 2016)

$$\boldsymbol{\sigma}_{\mathrm{S}} = \boldsymbol{\sigma}_{\mathrm{m}} + \frac{1}{N}\sum_{i=1}^{N}\left(\boldsymbol{\sigma}_{\mathrm{fe}}^i + \boldsymbol{\sigma}_{\mathrm{fd}}^i\right), \tag{8}$$

---

[2] For the membrane response to be quasi-isotropic, $N/2$ has to be an even integer.
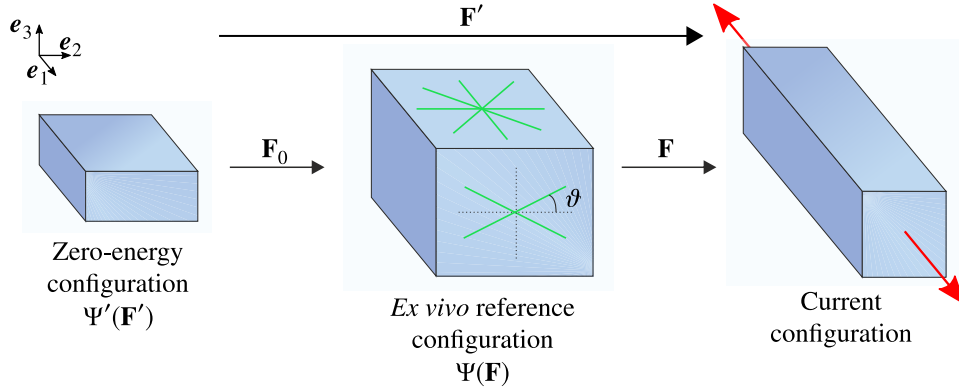
Fig. 2 Modeling concept for swelling tissues. Decomposition of the deformation gradient allows defining material parameters with respect to the known *ex vivo* reference configuration rather than the experimentally unknown zero-energy configuration. Projections of defined fiber orientations in-plane (top surface) and out-of-plane (front surface) are shown in green, together with the definition of the out-of-plane inclination angle ϑ

with the contributions

$$\boldsymbol{\sigma}_{\mathrm{m}} = \frac{\varphi_{\mathrm{S}}^{\mathrm{ref}}}{J} \mu_0 \mathrm{e}^{qg} m_1 \left(\mathbf{F} \mathbf{b}_0 \mathbf{F}^{\mathrm{T}} - (J J_0)^{-2m_2} \mathbf{I} \right), \tag{9a}$$

$$\boldsymbol{\sigma}_{\mathrm{fe}}^i = \frac{\varphi_{\mathrm{S}}^{\mathrm{ref}}}{J} \mu_0 \mathrm{e}^{qg} \frac{m_{\mathrm{fe}}}{\lambda_{\mathrm{fe}}^i} \langle \lambda_{\mathrm{fe}}^i - 1 \rangle^{2m_4-1} \boldsymbol{m}_{\mathrm{fe}}^i \otimes \boldsymbol{m}_{\mathrm{fe}}^i, \tag{9b}$$

$$\boldsymbol{\sigma}_{\mathrm{fd}}^i = \frac{\varphi_{\mathrm{S}}^{\mathrm{ref}}}{J} \mu_0 \mathrm{e}^{qg} \frac{m_{\mathrm{fd}}}{\lambda_{\mathrm{fd}}^i} \langle \lambda_{\mathrm{fd}}^i - 1 \rangle^{2m_4-1} \boldsymbol{m}_{\mathrm{fd}}^i \otimes \boldsymbol{m}_{\mathrm{fd}}^i. \tag{9c}$$

In this formulation, each fiber can be thought of as an elastic and a Maxwell element in parallel in the sense of a rheological scheme, for which the stored energy depends on the corresponding fiber stretches, $\lambda_{\mathrm{fe}}^i = \|\boldsymbol{m}_{\mathrm{fe}}^i\| = \lambda_{\mathrm{fe}}^{\mathrm{ref}} \|\mathbf{F}\boldsymbol{M}^i\|$ and $\lambda_{\mathrm{fd}}^i = \|\boldsymbol{m}_{\mathrm{fd}}^i\|$, respectively (*cf.* Nguyen et al., 2007). The fiber pre-stretch, $\lambda_{\mathrm{fe}}^{\mathrm{ref}}$, results from the free-swelling condition (Sec. 2.4.3), while $\boldsymbol{m}_{\mathrm{fd}}^i$ were treated as internal variables and computed from evolution equations (Mauri et al., 2016; Rubin and Bodner, 2002). Here, a similar form to that proposed by Mauri et al. (2016) was used,

$$\dot{\boldsymbol{m}}_{\mathrm{fd}}^i = \dot{\mathbf{F}} \mathbf{F}^{-1} \boldsymbol{m}_{\mathrm{fd}}^i - k_{\mathrm{fd}} \operatorname{tr}(\boldsymbol{\sigma}_{\mathrm{fd}}^i) \boldsymbol{m}_{\mathrm{fd}}^i, \tag{10}$$

with $k_{\mathrm{fd}} \operatorname{tr}(\boldsymbol{\sigma}_{\mathrm{fd}}^i)$ determining the dissipation rate of fiber i and k_{fd} being a positive material parameter.

The osmotic pressure was constitutively prescribed as (Stracuzzi et al., 2018)

$$\Delta \pi(J) = -\frac{\partial \Psi_{\mathrm{osm}}(J)}{\partial J} = \beta_0 \left(\frac{1 - \varphi_{\mathrm{S}}^{\mathrm{ref}}}{J - \varphi_{\mathrm{S}}^{\mathrm{ref}}} \right)^{\beta_1}, \tag{11}$$

with the parameters β_0 and $\beta_1 > 0$. For charged tissues, the osmotic potential arising from the Donnan equilibrium (Donnan, 1924) with a monovalent salt solution is typically adopted (Ehlers et al., 2009; Wilson et al., 2005a,b). Note that, under the assumption of low concentration of fixed charges compared to the osmolarity of the external bath, Eq. (11) can

be shown to relate to the ideal Donnan potential by choosing $\beta_0 = \frac{1}{4} R \Theta (c_{\mathrm{fc}}^{\mathrm{ref}})^2 / c_{\mathrm{ext}}$ and $\beta_1 = 2$ (*cf.* Lai et al., 1991); R being the ideal gas constant, Θ the absolute temperature, $c_{\mathrm{fc}}^{\mathrm{ref}}$ the fixed charge density in the *ex vivo* reference configuration, and c_{ext} the salt concentration of the external bath. A similar relationship between the two formulations can also be derived for very dilute solutions: $\beta_0 = R \Theta c_{\mathrm{fc}}^{\mathrm{ref}}$ and $\beta_1 = 1$.

A generalized Darcy's law was used to relate the IF flux to the gradient of the fluid chemical potential through the specific spatial permeability tensor $\mathbf{k}$ (Ehlers et al., 2009):

$$\boldsymbol{q} = -\mathbf{k} \operatorname{grad} \mu_{\mathrm{F}}. \tag{12}$$

Here, $\mathbf{k}$ was chosen spatially isotropic with the simple deformation-dependent form (Ateshian and Weiss, 2010; Markert, 2007)

$$\mathbf{k} = k(J)\mathbf{I}, \quad k(J) = k_0 \left(\frac{J - \varphi_{\mathrm{S}}^{\mathrm{ref}}}{1 - \varphi_{\mathrm{S}}^{\mathrm{ref}}} \right)^{\kappa}, \tag{13}$$

k_0 denoting the permeability in the *ex vivo* reference and $\kappa > 0$ a material parameter.

2.4.3 Reference configuration

Given the assumed fiber orientations in the *ex vivo* reference configuration, the hydrostatic stress due to osmotic pressure results in a free-swelling deformation gradient of the form $\mathbf{F}_0 = \lambda_{\mathrm{ip}}(\boldsymbol{e}_1 \otimes \boldsymbol{e}_1 + \boldsymbol{e}_2 \otimes \boldsymbol{e}_2) + \lambda_{\mathrm{op}} \boldsymbol{e}_3 \otimes \boldsymbol{e}_3$, λ_{ip} and λ_{op} being the stretches in-plane and out-of-plane, respectively. Free-swelling equilibrium requires $\boldsymbol{\sigma} = \mathbf{0}$ and $\mu_{\mathrm{F}} = 0$ for $\mathbf{F} = \mathbf{I}$. Noting that the evolution equations (10) drive the dissipative fiber contributions $\boldsymbol{\sigma}_{\mathrm{fd}}^i$ to zero, evaluating Eqs. (8), (9), and

(11) yields the equations

$$\varphi_S^{\text{ref}} \mu_0 e^{qg} \Big[m_1 \left(\lambda_{\text{ip}}^2 - J_0^{-2m_2} \right) +$$

$$\frac{1}{2} m_{\text{fe}} \sin^2 \theta \lambda_{\text{fe}}^{\text{ref}} \langle \lambda_{\text{fe}}^{\text{ref}} - 1 \rangle^{2m_4-1} \Big] - \beta_0 = 0, \quad (14\text{a})$$

$$\varphi_S^{\text{ref}} \mu_0 e^{qg} \Big[m_1 \left(\lambda_{\text{op}}^2 - J_0^{-2m_2} \right) +$$

$$m_{\text{fe}} \cos^2 \theta \lambda_{\text{fe}}^{\text{ref}} \langle \lambda_{\text{fe}}^{\text{ref}} - 1 \rangle^{2m_4-1} \Big] - \beta_0 = 0, \quad (14\text{b})$$

to be solved for λ_{ip} and λ_{op} under the volume fraction constraint $\varphi_S^{\text{ref}} J_0 \leq 1$, $J_0 = \lambda_{\text{ip}}^2 \lambda_{\text{op}}$. The fiber pre-stretch, $\lambda_{\text{fe}}^{\text{ref}}$, is determined in terms of λ_{ip}, λ_{op}, and the prescribed orientation in the *ex vivo* reference assuming fibers are unstretched in the zero-energy configuration. This condition can be written as $1 = \lambda_{\text{fe}}^{\text{ref}} \|\mathbf{F}_0^{-1} \boldsymbol{M}^i\|$, allowing the fiber pre-stretch to be evaluated as $\lambda_{\text{fe}}^{\text{ref}} = \left(\lambda_{\text{ip}}^{-2} \sin^2 \theta + \lambda_{\text{op}}^{-2} \cos^2 \theta \right)^{-1/2}$.

2.4.4 Finite element implementation

The model was implemented in the finite element software COMSOL Multiphysics® (COMSOL Multiphysics® 5.2a, COMSOL AB, Stockholm, Sweden). Due to symmetry, an eighth of the full uniaxial geometry was considered. The dimension in direction 1 (see Fig. 2) was reduced to obtain a thin slice along the loading direction. In fact, as IF flow is gradient-driven and the specimen is long compared to its width and thickness, gradients in the fluid chemical potential in loading direction can be neglected. A rectangular cuboid of dimensions $1.0 \times 2.5 \times 1.0 \, \text{mm}^3$ was discretized with hexahedral elements, employing quadratic and linear interpolation functions for the displacements and the fluid chemical potential, respectively. Both the normal displacement and fluid flux were prescribed to vanish on symmetry surfaces, while zero tractions and homogeneous Dirichlet conditions for the fluid chemical potential ($\mu_F = 0$) were applied to surfaces in contact with the external bath. In line with experimental realizations, monotonic tests were simulated by elongating the modeled domain at $0.001 \, \text{s}^{-1}$, whereas relaxation was realized by applying a ramp to 10 % elongation in 3 seconds and subsequently keeping the simulated domain at constant length. Changes in the osmolarity of the external bath during relaxation tests were simulated by updating the value of β_0 to $0.63 \, \text{kPa}$ ($0.60 \, \text{M}$ NaCl) or $5.44 \, \text{kPa}$ (distilled water) at the time-point of change of bath as applied in the experiments. Values of the solid volume fraction ($\varphi_S^{\text{ref}} = 0.30$, Nakagawa et al., 2010) and the reference permeability ($k_0 = 0.50 \, \text{mm}^4 \, \text{N}^{-1} \, \text{s}^{-1}$, Rutkowski and Swartz, 2007; Oftadeh et al., 2018) were chosen within the range reported in literature; the remaining material parameters were determined with the aim of providing a reasonable representation of both monotonic and relaxation experiments on human skin. Note that no extensive optimization procedure was performed to this end. The parameters used for all simulations are summarized in Table 2. For comparison, a nearly incompressible response (for the strain rates considered here) without osmotic effects was realized by letting $k_0 = 1 \times 10^{-6} \, \text{mm}^4 \, \text{N}^{-1} \, \text{s}^{-1}$ and $\beta_0 = 0 \, \text{kPa}$.

Table 2 Material parameters of the biphasic model for human skin used for representing both monotonic and relaxation behavior

μ_0	26.68	kPa	ϑ	10.0	$^\circ$
q	3.40		k_{fd}	1.43×10^{-2}	$\text{mm}^2 \, \text{N}^{-1} \, \text{s}^{-1}$
m_1	0.10		k_0	0.50	$\text{mm}^4 \, \text{N}^{-1} \, \text{s}^{-1}$
m_2	1.00		κ	2.00	
m_{fe}	250		β_0	2.49	kPa
m_{fd}	675		β_1	2.00	
m_4	1.40		φ_S^{ref}	0.30	

3 Results

3.1 Skin volume is reduced under uniaxial tension

Monotonic uniaxial tests confirm the typical J-shaped tension-stretch response (Fig. 3a), well-known for most soft biological tissues including human (Ní Annaidh et al., 2012b) and murine (Bancelin et al., 2015) skin, as well as pronounced contractions in the plane perpendicular to the loading direction (Fig. 3bc). Taken together, these results reveal a significant and increasing loss of volume with elongation for both skin types (Fig. 3d). Evaluating tangent Poisson's ratios ν_{12} and ν_{13} (Eq. (1)) for human skin gives values of 0.95 and 0.49 in the limit of infinitesimal strain, which increase up to 3.10 and 1.74 for $\lambda_1 = 1.20$; together, these results are interpreted as negative compressibility for solids (Baughman et al., 1998). Further, quantifying the elastic tensile moduli results in $(89 \pm 27) \, \text{kPa}$ and $(288 \pm 178) \, \text{kPa}$ for human and murine skin, respectively.

The reversibility of the observed deformation behavior was assessed in separate cyclic uniaxial tests. Representative curves of tension-stretch and in-plane kinematics for both skin types are reported in Fig. 4. Quantifying the maximum tangent Poisson's ratio ν_{12} within each loading cycle shows a consistent behavior, characterized by an initial decrease followed by a stabilization after repeated loading-unloading (Fig. 4e). While human tissue displays larger initial maximum ν_{12} than murine skin (3.30 ± 0.32 *vs.* 2.63 ± 0.51), both reach a value of approximately 2 after 5 cycles; this is much larger than the expected value of 0.5 for an isotropic incompressible solid. It is to be noted that the in-plane kinematics, or the Poisson's ratio derived therefrom, is by itself not sufficient to infer about the compressibility of materials of orthotropic or lesser symmetry.
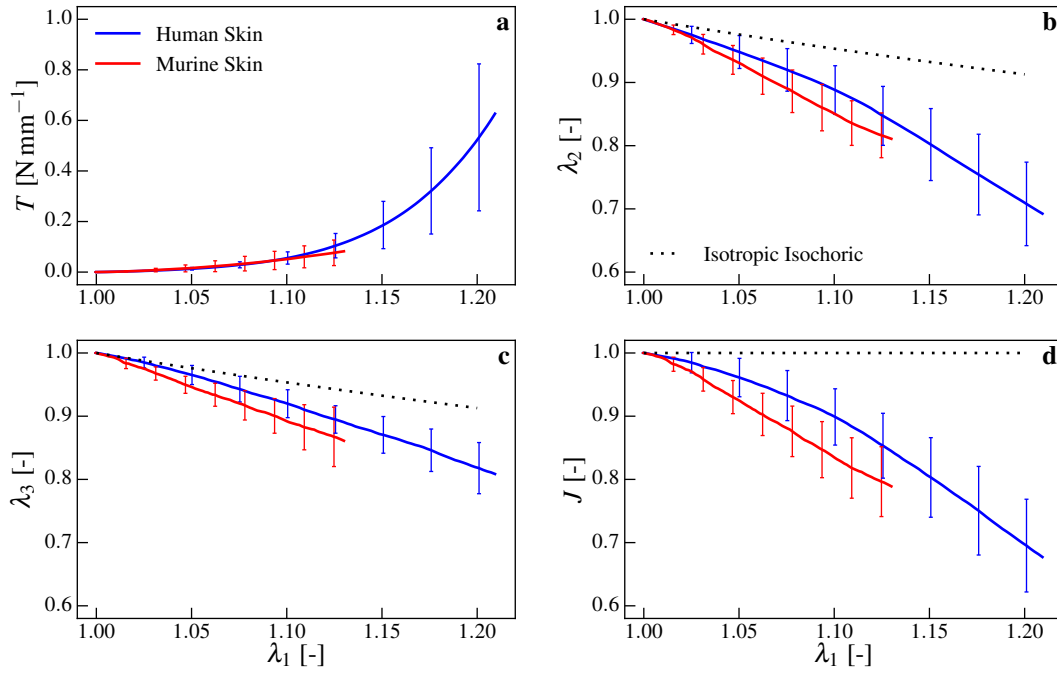
Fig. 3 Uniaxial tensile response of human and murine skin. Both skins are characterized by J-shaped tension-stretch curves (**a**), large lateral contractions in-plane (**b**) and out-of-plane (**c**), and volume loss (**d**) under uniaxial tension. For comparison, the dotted lines in (**b-d**) show the expected kinematics for an isotropic incompressible solid ($\lambda_2 = \lambda_3 = 1/\sqrt{\lambda_1}, J = 1$)
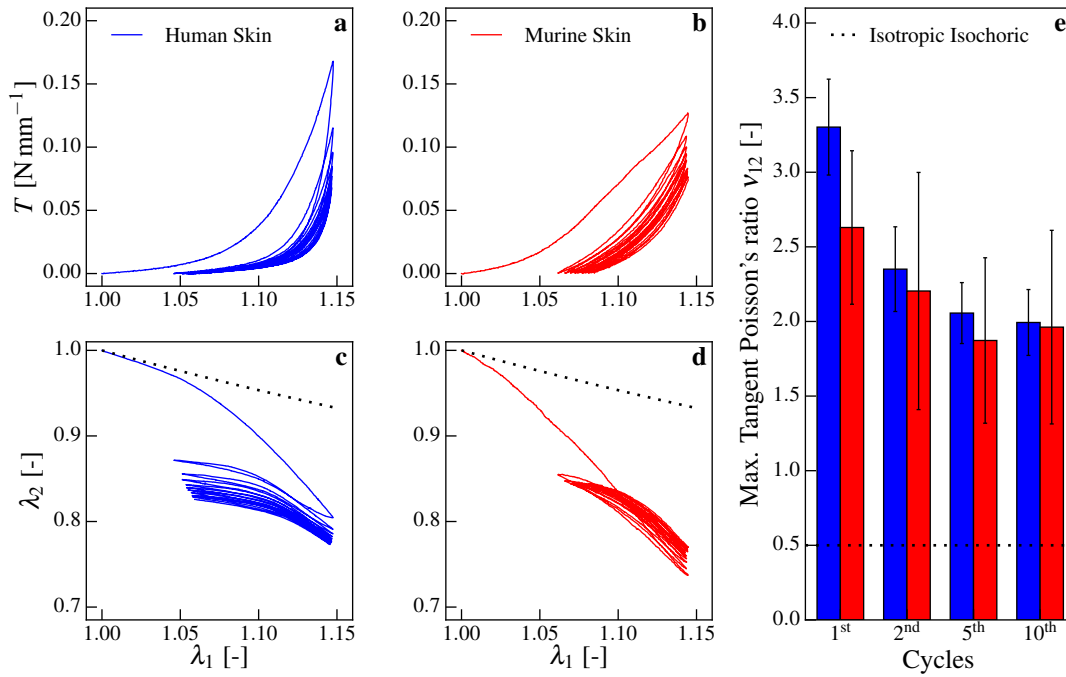

Fig. 4 Evolution of nominal tension and in-plane kinematics over successive cyclic uniaxial loading. Tension-stretch and in-plane kinematics are shown for representative experiments on human (**a**, **c**) and murine (**b**, **d**) skin. Maximum tangent Poisson's ratio ν_{12} (**e**) shows the deviation from isotropic incompressible solids ($\lambda_2 = 1/\sqrt{\lambda_1}$, $\nu_{12} = 0.5$; dotted lines in **c**, **d**, and **e**)

3.2 Human skin shows large *in vivo* lateral contraction

To assess the in-plane kinematics of human skin in physiological conditions, additional measurements were carried out on volar forearms *in vivo*. Despite some degree of constraint imposed by the surrounding tissue, a strong lateral contraction is seen in experiments performed on both volunteers' forearms (Fig. 5).
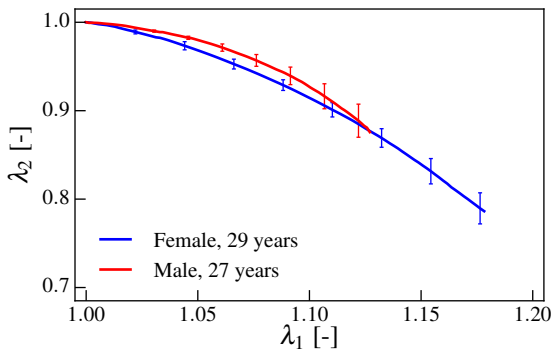

Fig. 5 Significant contraction in direction perpendicular to the applied elongation when stretching the skin surface of the volar forearm of the two volunteers ($n = 3$ repetitions)

Fig. 6 Relaxation experiments show chemo-mechanically coupled response: a change in bath osmolarity affects the tensile behavior. Both human skin (**a**) and murine skin (**b**) display qualitatively similar behavior with reversed relaxation after a change to distilled water (blue) and further decreased tension after a change to a hypertonic solution (red) compared to control experiments without change in bath osmolarity (black). Note the different scales in (**a**) and (**b**)

3.3 Changes in bath osmolarity modulate the relaxation behavior

The measured nominal tension in uniaxial relaxation experiments, normalized with respect to the value at the time point when change of bath was performed (T_{CoB}), is reported in Fig. 6a and Fig. 6b for human and murine skin, respectively. For both types of tissue, changes in the ionic environment clearly affect the evolution of tension over time, inducing effects that are qualitatively similar to expectations from Donnan theory (Donnan, 1924). Note the different time scales for human and murine skin, reflecting the difference in their thickness.
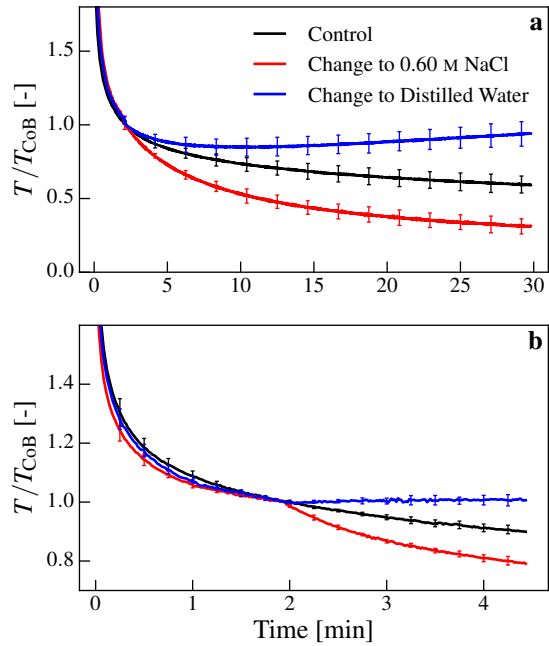
3.4 A biphasic model for human skin rationalizes the experimental observations

The monotonic uniaxial response predicted by the biphasic model is shown in Fig. 7. Comparison with the measurements on human skin reveals a fair agreement between model and experiments, particularly if compared with the prediction when simulating a nearly incompressible response. Clearly, the latter—or other suitable anisotropic incompressible models (see, *e.g.*, Latorre et al., 2016)—could be calibrated to give a close representation of the measured tension, and, for example, the in-plane kinematics, but not the complete deformation behavior, see Fig. 7cd.

The biphasic model is also able to represent the large and rapid stress relaxation observed for human skin (75 % over the first 2 minutes; Fig. 8a). The long-term progression, characterized by an evident tension reduction still visible at the end of the experiment, is instead not captured. While the model can qualitatively predict the effects of a change in bath osmolarity (Fig. 8b), the kinetics after such change show significant differences in comparison to the experiments (Fig. 6a); this is most evident when changing to hypotonic conditions.
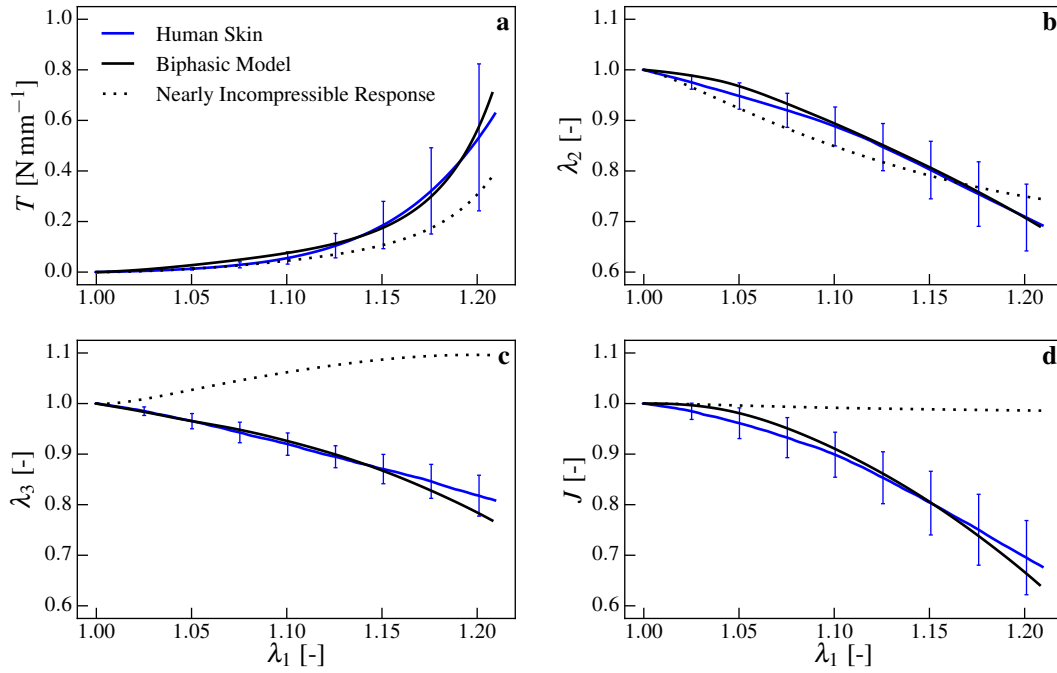
Fig. 7 Comparison of nominal tension (**a**), in-plane (**b**) and out-of-plane (**c**) lateral stretches, and volume ratio (**d**) for the biphasic model and the simulated nearly incompressible response with the corresponding experimental data for human skin
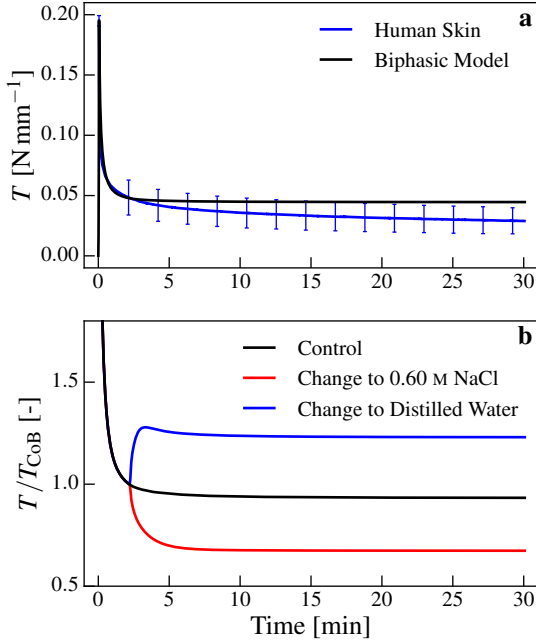

Fig. 8 Biphasic model fit to relaxation experiments on human skin. The model is able to reproduce the large short-term relaxation (**a**) and, qualitatively, the chemo-mechanically coupled response (**b**)

4 Discussion

Motivated by the increasing evidence of relevant cell-ECM interaction at the biophysical level, we investigated the link between mechanical stretch, IF mobility, and volume change in human and murine skin. By volume fraction, IF is the main constituent of skin and most soft connective tissues; however, due to its large bulk modulus compared to the low distortional stiffness of soft tissues (Vossoughi and Vaishnav, 1979), biomechanical models of the skin have typically assumed that the IF is bound and thus restricts the skin to undergo isochoric deformations (Buganza Tepole et al., 2014; Ehret et al., 2011; Hendriks et al., 2006; Limbert, 2011, 2017; Ní Annaidh et al., 2012a; Tonge et al., 2013b; Rubin and Bodner, 2002; Weickenmeier et al., 2015). Conversely, we have demonstrated that the volume of both human and murine skin is reduced under uniaxial tension (Fig. 3) due to efflux of IF. In particular, for human skin tissue, a 20 % elongation results in a decrease of the volume ratio J to ≈ 0.65, corresponding to a loss of half the amount of IF $((J - \varphi_S^{\text{ref}})/(1 - \varphi_S^{\text{ref}}) \approx 0.5)$. Furthermore, our results show that the mechanical response of skin depends on the osmolarity of the fluid environment (Fig. 6). This chemo-mechanically coupled tissue behavior implies that external forces not only affect the structural organization of the ECM, but also cause changes in osmotic and fluid hydrostatic pressure. For a 20 % elongation in 200 s, our model predicts that such changes amount to increases of 5.20 kPa

and 14.96 kPa in the center of the specimen compared to *ex vivo* reference conditions, respectively (data not shown).

4.1 Relevance for physiological conditions *in vivo*

To assess the relevance of these mechanisms for skin under physiological conditions, we complemented our extensive *ex vivo* campaign with a few experiments on human volar forearms *in vivo*. These showed that a strong lateral contraction is also evident when the tissue is deformed within its physiological environment (Fig. 5); interestingly, the measured values of lateral contraction are not excessively reduced when comparing *in vivo* with *ex vivo* uniaxial tests. We further used our biphasic model to predict the in-plane kinematics observed *in vivo* and the corresponding changes in IFP by discretizing a quarter of the stretched domain and surrounding tissue (Fig. 9ab). As the constraints imposed by the connected tissue are largely unknown, we analyzed the limiting cases of a free *vs.* fixed lateral boundary together with an intermediate case where the surface was constrained to half the displacements resulting from traction-free conditions. The top edge was displaced rapidly ($0.05\,\mathrm{s}^{-1}$) up to a 20 % elongation and subsequently kept constant to reveal the transient evolution of IFP. The bottom surface—physiologically attached to the underlying loose subcutaneous fat (Kolarsick et al., 2011)—was allowed to freely slide in the plane but kept fixed in the normal direction. Free fluid flow through the bottom surface was allowed. The top surface was modeled as traction-free and impermeable to fluid flow. Remarkably, the lateral contraction measured in our *in vivo* experiments falls well within the range predicted by the biphasic model (Fig. 9c). Moreover, the model predicts an almost isochoric response during the rapid stretching, as reflected by the large increase in fluid chemical potential (Fig. 9d), followed by fluid outflow, volume loss, and increased osmotic pressure; this highlights the effects caused by tissue extension *in vivo* due to IF mobility and chemo-mechanical coupling mechanisms.

Fig. 9 Prediction of planar kinematics and IFP in *in vivo* stretching experiments: (**a-b**) a quarter of the domain together with connected tissue was simulated, applying displacements $\hat{u}_1$ to the top edge and extracting the surface-averaged in-plane deformation gradient, as well as the values of p, μ_F, and $\Delta\pi$ in the center point P; (**c**) the experimentally observed large lateral contractions are well in line with model predictions; (**d**) rapid increase of fluid chemical potential and hydrostatic pressure during loading followed by relaxation and volume loss due to fluid outflow

4.2 Influence of reference criterion for experimental data analysis

Due to the low initial stiffness and highly nonlinear behavior of the skin, the criterion adopted to define the non-zero force level (*i.e.* the reference configuration) when analyzing experimental data may have a major influence on the reported tension-stretch as well as the kinematic response, as observed for other soft collagenous tissues (Bircher et al., 2016; Mauri et al., 2015a). We carefully selected low values of force threshold (human: 0.05 N; murine: 0.02 N, see Sec. 2.2.1), above sensor resolution and just sufficient to ensure taut samples. Although the relation between this *ex vivo* referenc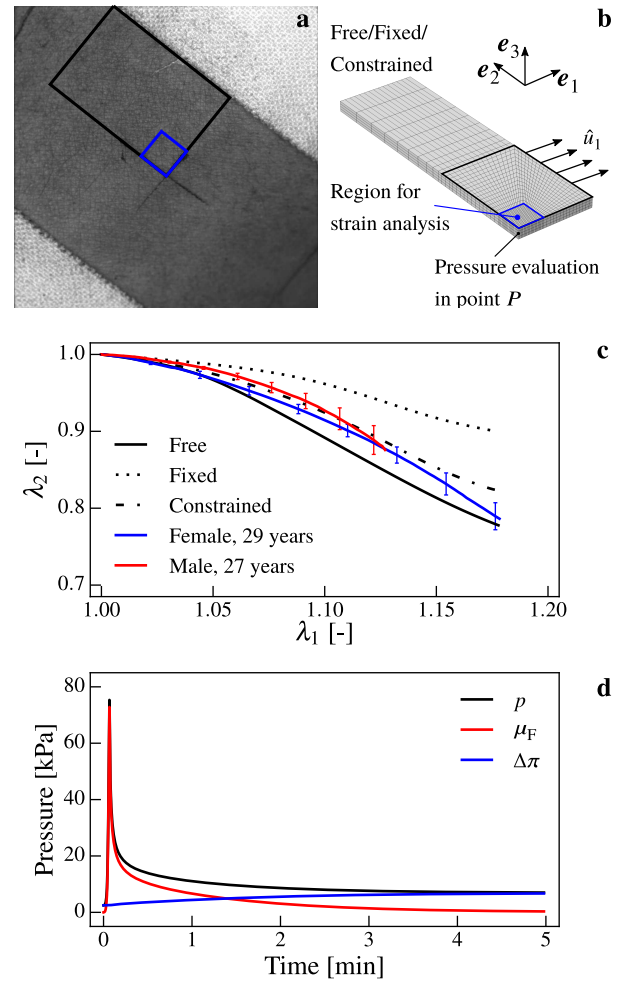e and the physiological conditions is unknown, an estimate of the physiological level of tension in murine skin *in vivo* ($0.025\,\mathrm{N\,mm}^{-1}$, Pensalfini et al., 2018) suggests that an *ex vivo* characterization has to be performed at such low forces to capture the behavior around the *in vivo* state and not only at supraphysiological conditions. In light of this, we note that our values of the elastic tensile modulus E for both human (89 kPa) and murine skin (288 kPa) are about one order of magnitude lower compared to corresponding values in literature obtained from uniaxial tension tests for each skin type (Ní Annaidh et al., 2012b; Rubin and Bodner, 2002; Muñoz et al., 2008). Besides obvious factors such as donor age, gender, ethnicity, and body location, as well as animal strain for mice, this significant discrepancy can be explained by differences in the chosen experimental reference criterion.

4.3 Implications for tissue function and mechanobiology

Extending the findings by Ehret et al. (2017), we have demonstrated that chemo-mechanically coupled tissue response, well-known for tissues like cartilage (*e.g.* Lai et al., 1991; Ateshian et al., 2009) and intervertebral disk (*e.g.* Frijns et al., 1997; Ehlers et al., 2009), is also a characteristic of skin function in humans and mice (Fig. 6). It is known that alterations in local hydration level, which in turn produce changes in pH and osmotic pressure (Gray et al., 1988; Loret and Simões, 2010), affect the proteoglycan deposition and GAG synthesis by chondrocytes in articular cartilage (Schneiderman et al., 1986; Gray et al., 1988; Quinn et al., 1998). Given the analogies in the multiphasic material behavior of the two tissues, these mechanically induced chemical variations may constitute relevant cues for the fibroblasts embedded in the dermis or for keratinocytes located near the dermo-epidermal interface. Evidence of a cellular response to IF flow (Ng et al., 2005; Rutkowski and Swartz, 2007) and pressure changes (Wiig et al., 2003), as well as to alterations in the osmotic pressure (Urban et al., 1993; Johnson et al., 2014), provides further support toward an active mechanobiological role of the chemo-mechanical coupling within soft connective tissue function. A thorough understanding of these aspects may contribute to the development and design of scaffolds for skin tissue engineering (Rosso et al., 2004; Metcalfe and Ferguson, 2007). In this context, establishing accurate constitutive models of the multiphasic response of soft biological tissues paves the way to clinically relevant *in silico* analyses of tissue behavior under physiological or pathological conditions, as well as of tissue remodeling during wound healing (Buganza Tepole, 2017).

4.4 Relevance of biphasic modeling for skin biomechanics

Modeling the complex, coupled biophysical characteristics of skin behavior presented here (Figs. 3 and 6) requires the inclusion of multiple phases and their interactions within a powerful theoretical framework such as the TPM (Ehlers, 2002). Our biphasic model represents a first step in this direction, allowing an analysis of changes in IF pressure and flow as well as osmotic pressure, in addition to the mechanical fields. In particular, the model has allowed us to produce first estimates of the magnitude of cell-relevant mechanically induced cues that arise from the multiphasic composition of skin tissue under *in vivo* loading conditions.

Noteworthy, the special case of nearly incompressible behavior is naturally included in TPM-based modeling approaches in the limiting case of rapid loading compared to the time scale of IF flow. The simplification offered by reduction to a monophasic incompressible model should however be critically assessed *a priori* based on estimates of material parameters and the specific boundary conditions under consideration; existing isochoric models of skin biomechanics might therefore be misleading.

4.5 Limitations

Our current work also has a few limitations, which need to be addressed and may suggest future developments. First, to study the deformation mechanisms of the skin, we focused on uniaxial rather than biaxial tensile tests. The skin does indeed experience biaxial rather than uniaxial tension under physiological loading *in vivo*, with the latter being important as representative of the near-field of a defect. We note that the interaction between the collagen fiber network and the IF has been found to lead to volume loss, albeit to a lesser extent, also in equibiaxial loading for other soft collagenous membranes (Ehret et al., 2017).

Second, we have neglected the fact that skin is comprised of several layers, each differing in structure and hosting different cell types. The expected lower permeability of the epidermis compared to the dermis would for example affect the flow paths and IFP distribution through the thickness, and may also induce (transient) structural effects. The differing mechanical properties of the individual layers (Crichton et al., 2011; Leyva-Mendivil et al., 2015) also contribute to structural effects, such as the significant edge bending observed in experiments on murine tissue; this influence was instead minor in human skin, possibly due to the larger thickness ratio between dermis and epidermis. Identification of the role of each layer is ongoing and will yield further insight into the biophysical environment of the cells, followed by corresponding improvements in the numerical model. Moreover, modeling the solid phase as a homogeneous, transversally isotropic matrix-fiber composite neglects the known in-plane anisotropy of the dermis (Ehret et al., 2011; Ní Annaidh et al., 2012b). Although motivated by the fact that IF is expected to flow primarily through the thickness due to the membrane geometry, the chosen spatially isotropic permeability model is a clear simplification. Corroborated by dedicated experiments, general anisotropic permeability models (Ateshian and Weiss, 2010), or models that explicitly take the microstructure of fiber-reinforced materials into account (Federico and Grillo, 2012; Tomic et al., 2014), may be used to better understand and model the hydraulic properties of the skin.

Third, we focused on relatively short time scales and the relaxation experiments clearly show that a steady-state behavior cannot be reached within a few minutes. By virtue of the assumption of immediate equilibrium of ions, change in bath osmolarity can only be qualitatively predicted unless the time constant for ion diffusion is short enough relative to other dissipative processes at play. In fact, comparing the characteristic time scale for ion diffusion, $\tau_{ion} \propto L^2/D$, and IF flow,

$\tau_F \propto L^2/(Ek)$, yields the relation $\tau_{ion}/\tau_F = Ek/D$ (Grodzinsky, 2011); L being a characteristic length and D the ion diffusion coefficient. Together with typical values of ion diffusivities in connective tissues (10^{-4} mm^2 s^{-1} to 10^{-3} mm^2 s^{-1}, Maroudas, 1968; Frijns et al., 1997; Gu et al., 2004), our values of $E \approx 0.1$ MPa and $k \approx 0.5$ mm^4 N^{-1} s^{-1} suggest that the time scale for ion diffusion might actually be *longer* than the time scale for IF flow (*cf.* Figs. 6a and 8b). Furthermore, we note that the difference in tension between control and hypertonic conditions by the end of the relaxation experiments is well captured by a change in β_0 deriving from a fixed charge density $c_{fc}^{ref} \approx 0.025$ M (*cf.* Sec. 2.4.2). However, this value together with Donnan equilibrium results in a large overprediction when simulating the change to distilled water (data not shown). A lack of mobile ions in the external bath can reduce the number of ionized groups of the proteoglycans (Ateshian et al., 2009), explaining this deviation. Further analysis should consider more advanced quadriphasic models (Huyghe and Janssen, 1997; Frijns et al., 1997) in the study of the kinetics after changes in bath osmolarity.

Finally, our *in vivo* measurements are limited to planar kinematics; thus, an assessment of the differences in boundary conditions when compared to *ex vivo* results is not possible. Further experimental analyses on poroelastic effects *in vivo* and corresponding relevant boundary conditions are therefore needed to enhance the proposed numerical model in view of application to *in vivo* conditions.

5 Conclusions

A series of monotonic, cyclic, and relaxation experiments was performed on human and murine skin, demonstrating the following properties: (i) skin is inverse poroelastic in that its volume decreases significantly while tensioned; (ii) corresponding lateral contractions are largest in-plane, with tangent Poisson's ratios for human skin reaching values up to 3.10 in monotonic tests and 2.06 after 5 loading cycles; (iii) skin shows a chemo-mechanically coupled response with significant tension modulation following a change in environmental osmolarity.

The proposed homogenized biphasic model is able to rationalize all main observed features. The model provides indications of changes in fluid chemical potential, fluid hydrostatic pressure, and osmotic stresses which might occur in case of skin tension, both *ex vivo* and *in vivo*. These changes are expected to provide relevant cues for dermal cells, thus influencing skin mechanobiology.

Compliance with ethical standards

Conflict of interest The authors declare that they have no conflict of interest.

Research involving human participants All experiments involving human participants and human tissue were approved by the local ethical committees; details are given in Sec. 2. Signed informed consent was provided from all participants and tissue donors.

References

Achterberg VF, Buscemi L, Diekmann H, Smith-Clerc J, Schwengler H, Meister JJ, Wenck H, Gallinat S, Hinz B (2014) The nano-scale mechanical properties of the extracellular matrix regulate dermal fibroblast function. J Invest Dermatol 134(7):1862–1872

Ateshian GA, Weiss JA (2010) Anisotropic hydraulic permeability under finite deformation. J Biomech Eng 132(11):111004

Ateshian GA, Rajan V, Chahine NO, Canal CE, Hung CT (2009) Modeling the matrix of articular cartilage using a continuous fiber angular distribution predicts many observed phenomena. J Biomech Eng 131(6):061003

Azeloglu EU, Albro MB, Thimmappa VA, Ateshian GA, Costa KD (2008) Heterogeneous transmural proteoglycan distribution provides a mechanism for regulating residual stresses in the aorta. Am J Physiol Heart Circ Physiol 294(3):H1197–H1205

Bader DL, Bowker P (1983) Mechanical characteristics of skin and underlying tissues in vivo. Biomaterials 4(4):305–308

Bancelin S, Lynch B, Bonod-Bidaud C, Ducourthial G, Psilodimitrakopoulos S, Dokládal P, Allain JM, Schanne-Klein MC, Ruggiero F (2015) Ex vivo multiscale quantitation of skin biomechanics in wild-type and genetically-modified mice using multiphoton microscopy. Sci Rep 5:1–14

Baughman RH, Stafström S, Cui C, Dantas SO (1998) Materials with negative compressibilities in one or more dimensions. Science 279(5356):1522–1524

Benítez JM, Montáns FJ (2017) The mechanical behavior of skin: Structures and models for the finite element analysis. Comput Struct 190:75–107

Bircher K, Ehret AE, Mazza E (2016) Mechanical characteristics of bovine Glisson's capsule as a model tissue for soft collagenous membranes. J Biomech Eng 138(8):081005

Brown AEX, Litvinov RI, Discher DE, Purohit PK, Weisel JW (2009) Multiscale mechanics of fibrin polymer: Gel

stretching with protein unfolding and loss of water. Science 325(5941):741–744

Brown IA (1973) A scanning electron microscope study of the effects of uniaxial tension on human skin. Br J Dermatol 89(4):383–393

Buerzle W, Mazza E (2013) On the deformation behavior of human amnion. J Biomech 46(11):1777–1783

Buganza Tepole A (2017) Computational systems mechanobiology of wound healing. Comput Meth Appl Mech Eng 314:46–70

Buganza Tepole A, Gosain AK, Kuhl E (2014) Computational modeling of skin: Using stress profiles as predictor for tissue necrosis in reconstructive surgery. Comput Struct 143:32–39

Crichton ML, Donose BC, Chen X, Raphael AP, Huang H, Kendall MAF (2011) The viscoelastic, hyperelastic and scale dependent behaviour of freshly excised individual skin layers. Biomaterials 32(20):4670–4681

Daly CH (1982) Biomechanical properties of dermis. J Invest Dermatol 79:48–51

Donnan FG (1924) The theory of membrane equilibria. Chem Rev 1(1):73–90

Ehlers W (2002) Foundations of multiphasic and porous materials. In: Ehlers W, Bluhm J (eds) Porous Media, Springer Berlin Heidelberg, pp 3–86

Ehlers W, Karajan N, Markert B (2009) An extended biphasic model for charged hydrated tissues with application to the intervertebral disc. Biomech Model Mechanobiol 8(3):233–251

Ehret AE, Hollenstein M, Mazza E, Itskov M (2011) Porcine dermis in uniaxial cyclic loading: Sample preparation, experimental results and modeling. J Mech Mater Struct 6(7-8):1125–1135

Ehret AE, Bircher K, Stracuzzi A, Marina V, Zündel M, Mazza E (2017) Inverse poroelasticity as a fundamental mechanism in biomechanics and mechanobiology. Nat Commun 8(1):1–9

Eskandari M, Kuhl E (2015) Systems biology and mechanics of growth. Wiley Interdiscip Rev Syst Biol Med 7(6):401–412

Federico S, Grillo A (2012) Elasticity and permeability of porous fibre-reinforced materials under large deformations. Mech Mater 44:58–71

Frijns AJH, Huyghe JM, Janssen JD (1997) A validation of the quadriphasic mixture theory for intervertebral disc tissue. Int J Eng Sci 35(15):1419–1429

Gibson T, Kenedi RM, Craik JE (1965) The mobile micro-architecture of dermal collagen: A bio-engineering study. Br J Surg 52(10):764–770

Gray ML, Pizzanelli AM, Grodzinsky AJ, Lee RC (1988) Mechanical and physicochemical determinants of the chondrocyte biosynthetic response. J Orthop Res 6(6):777–792

Grodzinsky AJ (2011) Fields, Forces and Flows in Biological Systems. Garland Science, New York

Groves RB, Coulman SA, Birchall JC, Evans SL (2013) An anisotropic, hyperelastic model for skin: Experimental measurements, finite element modelling and identification of parameters for human and murine skin. J Mech Behav Biomed Mater 18:167–180

Gu WY, Yao H, Vega AL, Flagler D (2004) Diffusivity of ions in agarose gels and intervertebral disc: Effect of porosity. Ann Biomed Eng 32(6):1710–1717

Guilak F, Cohen DM, Estes BT, Gimble JM, Liedtke W, Chen CS (2009) Control of stem cell fate by physical interactions with the extracellular matrix. Cell Stem Cell 5(1):17–26

Har-Shai Y, Bodner SR, Egozy-Golan D, Lindenbaum E, Ben-Izhak O, Mitz V, Hirshowitz B (1996) Mechanical properties and microstructure of the superficial musculoaponeurotic system. Plast Reconstr Surg 98:59–70

Hendriks FM, Brokken D, Oomens CWJ, Bader DL, Baaijens FPT (2006) The relative contributions of different skin layers to the mechanical behavior of human skin in vivo using suction experiments. Med Eng Phys 28(3):259–266

Hollenstein M, Ehret AE, Itskov M, Mazza E (2011) A novel experimental procedure based on pure shear testing of dermatome-cut samples applied to porcine skin. Biomech Model Mechanobiol 10(5):651–661

Hong W, Liu Z, Suo Z (2009) Inhomogeneous swelling of a gel in equilibrium with a solvent and mechanical load. Int J Solids Struct 46(17):3282–3289

Hopf R, Bernardi L, Menze J, Zündel M, Mazza E, Ehret AE (2016) Experimental and theoretical analyses of the age-dependent large-strain behavior of Sylgard 184 (10:1) silicone elastomer. J Mech Behav Biomed Mater 60:425–437

Humphrey JD, Dufresne ER, Schwartz MA (2014) Mechanotransduction and extracellular matrix homeostasis. Nat Rev Mol Cell Biol 15(12):802–812

Huyghe JM, Janssen JD (1997) Quadriphasic mechanics of swelling incompressible porous media. Int J Eng Sci 35(8):793–802

Imai SI (2009) The NAD world: A new systemic regulatory network for metabolism and aging-Sirt1, systemic NAD biosynthesis, and their importance. Cell Biochem Biophys 53(2):65–74

Jayyosi C, Affagard JS, Ducourthial G, Bonod-Bidaud C, Lynch B, Bancelin S, Ruggiero F, Schanne-Klein MC, Allain JM, Bruyère-Garnier K, Coret M (2017) Affine kinematics in planar fibrous connective tissues: an experimental investigation. Biomech Model Mechanobiol 16(4):1459–1473

Johnson ZI, Shapiro IM, Risbud MV (2014) Extracellular osmolarity regulates matrix homeostasis in the intervertebral disc and articular cartilage: Evolving role of TonEBP. Matrix Biol 40:10–16

Kitano H (2002) Computational systems biology. Nature 420(6912):206–210

Kolarsick PAJ, Kolarsick MA, Goodwin C (2011) Anatomy and physiology of the skin. J Dermatol Nurses Assoc 3(4):203–213

Lai WM, Hou JS, Mow VC (1991) A triphasic theory for the swelling and deformation behaviors of articular cartilage. J Biomech Eng 113(3):245

Lake SP, Barocas VH (2011) Mechanical and structural contribution of non-fibrillar matrix in uniaxial tension: A collagen-agarose co-gel model. Ann Biomed Eng 39(7):1891–1903

Lanir Y (1987) Biorheology and fluid flux in swelling tissues. I. Bicomponent theory for small deformations, including concentration effects. Biorheology 24(2):173–187

Lanir Y (2017) Multi-scale structural modeling of soft tissues mechanics and mechanobiology. J Elast 129(1-2):7–48

Lanir Y, Fung YC (1974) Two-dimensional mechanical properties of rabbit skin-II. Experimental results. J Biomech 7(2)

Latorre M, Romero X, Montáns FJ (2016) The relevance of transverse deformation effects in modeling soft biological tissues. Int J Solids Struct 99:57–70

Leyva-Mendivil MF, Page A, Bressloff NW, Limbert G (2015) A mechanistic insight into the mechanical role of the stratum corneum during stretching and compression of the skin. J Mech Behav Biomed Mater 49:197–219

Limbert G (2011) A mesostructurally-based anisotropic continuum model for biological soft tissues–decoupled invariant formulation. J Mech Behav Biomed Mater 4(8):1637–1657

Limbert G (2017) Mathematical and computational modelling of skin biophysics: a review. Proc R Soc A 473:20170257

Loret B, Simões FMF (2010) Effects of the pH on the mechanical behavior of articular cartilage and corneal stroma. Int J Solids Struct 47(17):2201–2214

Lucantonio A, Nardinocchi P, Teresi L (2013) Transient analysis of swelling-induced large deformations in polymer gels. J Mech Phys Solids 61(1):205–218

Lukashev ME, Werb Z (1998) ECM signalling: Orchestrating cell behaviour and misbehaviour. Trends Cell Biol 8(11):437–441

Mak AFT, Huang L, Wang Q (1994) A biphasic poroelastic analysis of the flow dependent subcutaneous tissue pressure and compaction due to epidermal loadings: Issues in pressure sore. J Biomech Eng 116(4):421

Markert B (2007) A constitutive approach to 3-d nonlinear fluid flow through finite deformable porous continua. Transp Porous Media 70(3):427–450

Maroudas A (1968) Physicochemical properties of cartilage in the light of ion exchange theory. Biophys J 8(5):575–595

Maroudas A (1976) Balance between swelling pressure and collagen tension in normal and degenerate cartilage. Nature 260:808–809

Mauri A, Ehret AE, Perrini M, Maake C, Ochsenbein-Kölble N, Ehrbar M, Oyen ML, Mazza E (2015a) Deformation mechanisms of human amnion: Quantitative studies based on second harmonic generation microscopy. J Biomech 48(9):1606–1613

Mauri A, Perrini M, Ehret AE, De Focatiis DSA, Mazza E (2015b) Time-dependent mechanical behavior of human amnion: Macroscopic and microscopic characterization. Acta Biomater 11(1):314–323

Mauri A, Ehret AE, De Focatiis DSA, Mazza E (2016) A model for the compressible, viscoelastic behavior of human amnion addressing tissue variability through a single parameter. Biomech Model Mechanobiol 15(4):1005–1017

Metcalfe AD, Ferguson MWJ (2007) Tissue engineering of replacement skin: The crossroads of biomaterials, wound healing, embryonic development, stem cells and regeneration. J R Soc Interface 4(14):413–417

Mouw JK, Ou G, Weaver VM (2014) Extracellular matrix assembly: A multiscale deconstruction. Nat Rev Mol Cell Biol 15(12):771–785

Muñoz MJ, Bea JA, Rodríguez JF, Ochoa I, Grasa J, Pérez del Palomar A, Zaragoza P, Osta R, Doblaré M (2008) An experimental study of the mouse skin behaviour: Damage and inelastic aspects. J Biomech 41(1):93–99

Nakagawa N, Matsumoto M, Sakai S (2010) In vivo measurement of the water content in the dermis by confocal raman spectroscopy. Skin Res Technol 16(2):137–141

Ng CP, Hinz B, Swartz MA (2005) Interstitial fluid flow induces myofibroblast differentiation and collagen alignment in vitro. J Cell Sci 118(20):4731–4739

Nguyen TD, Jones RE, Boyce BL (2007) Modeling the anisotropic finite-deformation viscoelastic behavior of soft fiber-reinforced composites. Int J Solids Struct 44(25-26):8366–8389

Ní Annaidh A, Bruyère K, Destrade M, Gilchrist MD, Maurini C, Otténio M, Saccomandi G (2012a) Automated estimation of collagen fibre dispersion in the dermis and its contribution to the anisotropic behaviour of skin. Ann Biomed Eng 40(8):1666–1678

Ní Annaidh A, Bruyère K, Destrade M, Gilchrist MD, Otténio M (2012b) Characterization of the anisotropic mechanical properties of excised human skin. J Mech Behav Biomed Mater 5(1):139–148

North JF, Gibson F (1978) Volume compressibility of human abdominal skin. J Biomech 11(4)

Oftadeh R, Connizzo BK, Nia HT, Ortiz C, Grodzinsky AJ (2018) Biological connective tissues exhibit viscoelastic and poroelastic behavior at different frequency regimes: Application to tendon and skin biophysics. Acta Biomater 70:249–259

Oomens CWJ, van Campen DH, Grootenboer HJ (1987) A mixture approach to the mechanics of skin. J Biomech

20(9):877–885

Page-McCaw A, Ewald AJ, Werb Z (2007) Matrix metallo-proteinases and the regulation of tissue remodelling. Nat Rev Mol Cell Biol 8(3):221–233

Pensalfini M, Haertel E, Hopf R, Wietecha M, Werner S, Mazza E (2018) The mechanical fingerprint of murine excisional wounds. Acta Biomater 65:226–236

Picu RC, Deogekar S, Islam MR (2018) Poisson's contrac-tion and fiber kinematics in tissue: Insight from collagen network simulations. J Biomech Eng 140(2):021002

Quinn TM, Grodzinsky AJ, Buschmann MD, Kim YJ, Hun-ziker EB (1998) Mechanical compression alters proteogly-can deposition and matrix deformation around individual cells in cartilage explants. J Cell Sci 111:573–583

Rosso F, Giordano A, Barbarisi M, Barbarisi A (2004) From cell-ECM interactions to tissue engineering. J Cell Physiol 199(2):174–180

Rubin MB, Bodner SR (2002) A three-dimensional nonlinear model for dissipative response of soft tissue. Int J Solids Struct 39(19):5081–5099

Rutkowski JM, Swartz MA (2007) A driving force for change: interstitial flow as a morphoregulator. Trends Cell Biol 17(1):44–50

Schneiderman R, Keret D, Maroudas A (1986) Effects of me-chanical and osmotic pressure on the rate of glycosamino-glycan synthesis in the human adult femoral head cartilage: An in vitro study. J Orthop Res 4(4):393–408

Smith CW, Wootton RJ, Evans KE (1999) Interpretation of experimental data for Poisson's ratio of highly nonlinear materials. Exp Mech 39(4):356–362

Stark HL, Al-Haboubi A (1980) The relationship of width, thickness, volume and load to extension for human skin in vitro. Eng Med 9(4):179–183

Stracuzzi A, Mazza E, Ehret AE (2018) Chemomechanical models for soft tissues based on the reconciliation of porous media and swelling polymer theories. Z Angew Math Mech 98(12):2135–2154

Tomic A, Grillo A, Federico S (2014) Poroelastic materials reinforced by statistically oriented fibres–numerical im-plementation and application to articular cartilage. IMA J Appl Math 79(5):1027–1059

Tonge TK, Atlan LS, Voo LM, Nguyen TD (2013a) Full-field bulge test for planar anisotropic tissues: Part I–Experimental methods applied to human skin tissue. Acta Biomater 9(4):5913–5925

Tonge TK, Voo LM, Nguyen TD (2013b) Full-field bulge test for planar anisotropic tissues: Part II–A thin shell method for determining material parameters and comparison of two distributed fiber modeling approaches. Acta Biomater 9(4):5926–5942

Tracy LE, Minasian RA, Caterson EJ (2016) Extracellular matrix and dermal fibroblast function in the healing wound. Adv Wound Care 5(3):119–136

Urban JP, Hall AC, Gehl KA (1993) Regulation of matrix synthesis rates by the ionic and osmotic environment of articular chondrocytes. J Cell Physiol 154(2):262–270

Veronda DR, Westmann RA (1970) Mechanical characteriza-tion of skin–Finite deformations. J Biomech 3(1):111–124

Vossoughi J, Vaishnav RN (1979) Comments on the paper "Volume compressibility of human abdominal skin". J Biomech 12:481

Wang J, Zhang Y, Zhang N, Wang C, Herrler T, Li Q (2015) An updated review of mechanotransduction in skin disorders: Transcriptional regulators, ion channels, and microRNAs. Cell Mol Life Sci 72(11):2091–2106

Weickenmeier J, Jabareen M, Mazza E (2015) Suction based mechanical characterization of superficial facial soft tissues. J Biomech 48(16):4279–4286

Wiig H, Rubin K, Reed RK (2003) New and active role of the interstitium in control of interstitial fluid pressure: potential therapeutic consequences. Acta Anaesthesiol Scand 47:111–121

Wilson W, van Donkelaar CC, Huyghe JM (2005a) A com-parison between mechano-electrochemical and biphasic swelling theories for soft hydrated tissues. J Biomech Eng 127(1):158

Wilson W, van Donkelaar CC, van Rietbergen B, Huiskes R (2005b) A fibril-reinforced poroviscoelastic swelling model for articular cartilage. J Biomech 38(6):1195–1204

Wong WLE, Joyce TJ, Goh KL (2016) Resolving the vis-coelasticity and anisotropy dependence of the mechanical properties of skin from a porcine model. Biomech Model Mechanobiol 15(2):433–446

Woo SL, Lubock P, Gomez MA, Jemmott GF, Kuei SC, Akeson WH (1979) Large deformation nonhomogeneous and directional properties of articular cartilage in uniaxial tension. J Biomech 12(6):437–446